Topological Circular Dichroism in Chiral Multifold Semimetals

Junyeong Ahn [1,*] and Barun Ghosh [2,†]

[1]*Department of Physics, Harvard University, Cambridge, Massachusetts 02138, USA*
[2]*Department of Physics, Northeastern University, Boston, Massachusetts 02115, USA*

Uncovering the physical contents of the nontrivial topology of quantum states is a critical problem in condensed matter physics. Here, we study the topological circular dichroism in chiral semimetals using linear response theory and first-principles calculations. We show that, when the low-energy spectrum respects emergent SO(3) rotational symmetry, topological circular dichroism is forbidden for Weyl fermions, and thus is unique to chiral multifold fermions. This is a result of the selection rule that is imposed by the emergent symmetry under the combination of particle-hole conjugation and spatial inversion. Using first-principles calculations, we predict that topological circular dichroism occurs in CoSi for photon energy below about 0.2 eV. Our Letter demonstrates the existence of a response property of unconventional fermions that is fundamentally different from the response of Dirac and Weyl fermions, motivating further study to uncover other unique responses.

Introduction.—The interaction between chiral materials and circularly polarized light is a topic of broad interest in fundamental sciences [1–10]. Because chiral materials have a definite left- or right-handed crystalline structure, they respond differently to the left and right circularly polarized light. Natural optical activity (i.e., optical rotation and circular dichroism with time-reversal symmetry) and the circular photogalvanic effect are such phenomena due to the light-helicity dependence in the refractive index and dc photocurrent, respectively.

The quantization of the circular photogalvanic effect in chiral topological semimetals has gained attention recently [7–9,11–13]. In three-dimensional chiral crystals, a band-crossing point carries a quantized magnetic monopole charge in momentum space, which is the Chern number [14,15]. While the magnetic monopoles appear in pairs in the Brillouin zone by the fermion doubling theorem [16], monopole and antimonopole are not at the same energy, in general, because there is no symmetry to relate them in chiral crystals. The uncompensated monopole charge of a chiral fermion near the Fermi level can manifest through physical responses. The quantized circular photogalvanic effect is a rare example of topological optical responses originating from the monopole charge of a chiral fermion.

More recently, another topological optical phenomenon was discovered in chiral topological semimetals [17,18]. It was proposed that linearly dispersing chiral fermions show topological circular dichroism, where the helicity-dependent absorption of light is determined only by universal quantities, including fundamental constants and the ratio between the sample thickness and the light wavelength [Fig. 1]. While this discovery provides another

exciting example of topological optical responses, the results in Refs. [17,18] need further investigation because they were derived from physical arguments using Fermi's Golden rule without rigorous derivations.

In this Letter, we investigate topological circular dichroism in chiral topological semimetals using linear response theory and first-principles calculations. Remarkably, we find that topological circular dichroism does not appear for Weyl fermions, which are chiral fermions with twofold degenerate band-crossing points, and is thus unique to chiral multifold fermions having threefold or fourfold degenerate band-crossing points. We also find differences in the magnitude and spectral range of the quantized response for chiral multifold fermions compared to the original proposal. We show that these new features are mainly because of the selection rule imposed by the symmetry under the combination of particle-hole conjugation and spatial inversion.

Unlike the quantized circular photogalvanic effect, topological circular dichroism does not depend on the current relaxation time, which depends on materials. Instead, the topological circular dichroism relies on isotropic linear dispersion. To test our model analysis, we perform first-principles calculations of the circular dichroism for CoSi, a chiral threefold semimetal with good linear dispersions per spin degrees of freedom [19–23]. The result agrees well with model analysis, showing approximate quantizations for photon energies below about 0.2 eV.

Isotropic k dot p model.—We first consider the model of isotropic chiral pseudospin-j fermions in three dimensions [14,20].

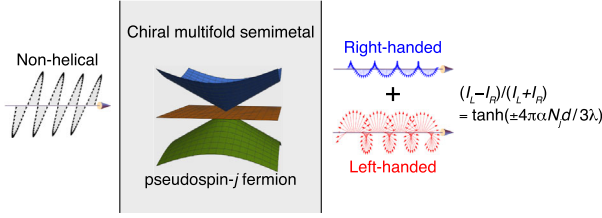$$H_0(\mathbf{k}) = -\mu + \chi v \mathbf{k} \cdot \mathbf{J}, \tag{1}$$

FIG. 1. Topological circular dichroism by a chiral multifold semimetal hosting a pseudospin-j fermion near the Fermi level. $I_{L/R}$s are the transmitted intensity for the left (L) and right (R) handed light. $N_{1/2} = 0$, $N_1 = 1$, and $N_{3/2} = 3$.

where **k** is the wave vector, **J** is the pseudospin-j operator satisfying the su(2) algebra because of isotropy. The sign $\chi = \pm 1$ determines the chirality. The energy eigenvalues are

$$E_n(\mathbf{k}) = -\mu + \hbar v k h_n, \qquad (2)$$

where the integer $h_n = -j, \ldots, j$ is the helicity quantum number [Fig. 2]. The crossing point at $\mathbf{k} = 0$ has $(2j + 1)$-fold degeneracy. The band with helicity h carries the Chern number $c_h = -2\chi h$ on a closed surface that encloses the node (i.e., the magnetic monopole charge in momentum space defined by the Berry curvature), which serves as a topological charge of the spin-j fermion. We have a Weyl fermion for $j = 1/2$ and a chiral multifold fermion for a higher j. In this model, optical transitions occur between adjacent energy levels only because of an optical selection rule imposed by isotropy [19,24]: for $m \neq n$, transition dipole moment $\langle \psi_{m\mathbf{k}} | e\hat{\mathbf{r}} | \psi_{n\mathbf{k}} \rangle \propto \langle u_{m\mathbf{k}} | \mathbf{J} | u_{n\mathbf{k}} \rangle = 0$ if $h_m \neq h_n \pm 1$.

Our model has symmetry $TH(\mathbf{k})T^{-1} = H(-\mathbf{k})$ under effective time reversal T that flips the pseudospin. Therefore, the anomalous Hall effect is forbidden. However, natural optical activity can arise from broken inversion symmetry.
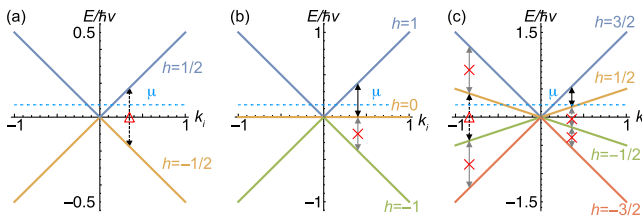

FIG. 2. Band structure of pseudospin-j fermions described by Eq. (1). (a) $j = 1/2$. (b) $j = 1$. (c) $j = 3/2$. The spectrum has the same shape along $k_{i=x,y,z}$ because of isotropy. Arrows represent possible optical transition channels allowed by the selection rule due to isotropy [19,24]. Optical transitions with red x marks are forbidden by the Pauli blocking with the chemical potential represented by the blue dashed line. CP symmetry further constrains that transitions between $h = \pm 1/2$ bands (arrows with red triangles) does not contribute to natural optical activity.

Below, we focus on isotropic spin-1 fermions because they are more relevant to real materials but consider spin-3/2 fermions as well for completeness. In crystals, the topological protection of multifold fermions requires particular space group symmetries. When spin-orbit coupling is negligible, space groups 195–199 and 207–214 combined with time reversal symmetry can protect isotropic threefold fermions [14]. A topologically stable isotropic threefold fermion can also appear in spin-orbit coupled antiferromagnets with type IV magnetic space groups $P_I 213(198.11)$, $P_I 4_3 32(212.62)$, and $P_I 4_1 32(213.66)$ [25]. On the other hand, a threefold fermion stabilized by other space group symmetries does not respect full isotropy in the low-energy limit [14,25]. Topologically protected spin-3/2 fermions do not have isotropy unless fine-tuned [14]. Nevertheless, we do not exclude the possibility of a fine-tuned isotropic spin-3/2 fermion and consider both isotropic spin-1 and spin-3/2 fermions.

Topological circular dichroism from natural optical activity.—In crystalline solids, natural optical activity is described by the part of the optical conductivity that is linear in photon momentum **q** [4]. Let us consider the expansion $\sigma_{ab}(\omega, \mathbf{q}) = \sigma_{ab}(\omega) + \sigma_{abc}(\omega)q_c + O(q^2)$. In our model, the refractive indices for light with left (L) and right (R) helicity are

$$n_{L/R} = \sqrt{1 + \chi_{xx} + (\mu_0 c \sigma_{xyz}/2)^2} \pm \mu_0 c \sigma_{xyz}/2, \quad (3)$$

where $\chi_{ab} = \sigma_{ab}(-i\epsilon_0 \omega)^{-1}$ is the electric susceptibility, and the light helicity is defined by the sign of $\mathbf{q} \cdot i\mathbf{E}^* \times \mathbf{E}$. For $\mathbf{q} = |\mathbf{q}|(0,0,1)$, L and R polarization vectors are, respectively, $\hat{L} = (1, -i, 0)/\sqrt{2}$ and $\hat{R} = (1, i, 0)/\sqrt{2}$. Because of the isotropy in our model, χ_{xx} and σ_{xyz} are the only nonvanishing tensor components. The real and imaginary parts of circular birefringence $n_L - n_R = \mu_0 c \sigma_{xyz}$ are responsible for the optical rotation and circular dichroism, respectively.

Natural optical activity has two contributions from the Fermi sea and the Fermi surface, respectively [4,5,26]. The formula for the Fermi sea part is [4]

$$\sigma_{abc}^0 = \frac{e^2 \omega}{\hbar} \sum_{n,m} \int_{\mathbf{k}} f_{nm} \left[\frac{\text{Im}(r_{nm}^a B_{mn}^{bc} - r_{nm}^b B_{mn}^{ac})}{\omega_{mn}^2 - \omega^2} - \frac{(3\omega_{mn}^2 - \omega^2)\text{Im}(r_{nm}^a r_{mn}^b)(v_{mm}^c + v_{nn}^c)}{2(\omega_{mn}^2 - \omega^2)^2} \right], \qquad (4)$$

where $\int_{\mathbf{k}} = \int_{\text{BZ}} d^3 k/(2\pi)^3$, $f_{nm} = f_n - f_m$ and $\hbar \omega_{mn} = \hbar \omega_m - \hbar \omega_n$ are the differences of the Fermi-Dirac distributions and energy eigenvalues, respectively, $v_{mn}^i = \langle \psi_{m\mathbf{k}} | \hat{v}^i | \psi_{n\mathbf{k}} \rangle$ and $r_{nm}^j = -iv_{nm}^j/\omega_{nm}$ are velocity and position matrix elements, $B_{mn}^{ab} = B_{mn}^{\text{orb},ab} + B_{mn}^{\text{spin},ab}$, $B_{mn}^{\text{orb},ab} = 2^{-1}(\sum_{p;E_p \neq E_m} r_{mp}^b v_{pn}^a + \sum_{p;E_p \neq E_n} v_{mp}^a r_{pn}^b)$,

$B_{mn}^{\text{spin},ab} = e^{-1}\epsilon_{abc}\langle\psi_{m\mathbf{k}}|\hat{M}^{\text{spin},c}|\psi_{n\mathbf{k}}\rangle$, and $\hat{\mathbf{M}}^{\text{spin}}$ is the spin magnetic moment operator. The spin magnetic moment does not contribute to the response in systems with negligible spin-orbit coupling; we discuss its effect in spin-orbit coupled systems below. The Fermi surface part is given by [5,27]

$$\sigma_{abc}^{G} = \frac{e^2}{\hbar}\sum_n\int_{\mathbf{k}}\left[\frac{1}{\omega}(\partial_a f_n B_{nn}^{bc} - \partial_b f_n B_{nn}^{ac})\right.$$
$$\left. - \partial_c f_n\sum_m\text{Im}(r_{nm}^a r_{mn}^b)\frac{\omega_{mn}\omega}{\omega_{mn}^2 - \omega^2}\right]. \quad (5)$$

The effect of dissipation is included by the substitution $\omega \to \omega + i\tau^{-1}$.

In the clean limit where $\omega\tau \to \infty$, the Fermi sea part is purely imaginary and thus describes circular dichroism.

$$\sigma_{abc}^{0} = \frac{i\pi e^2\omega}{\hbar}\sum_{\substack{n=\text{occ}\\m=\text{unocc}}}\int_{\mathbf{k}}\delta(\omega_{mn}-\omega)\times\text{Im}$$
$$\times\left[(r_{nm}^a B_{mn}^{bc} - r_{nm}^b B_{mn}^{ac} - \frac{1}{2}(r_{nm}^a r_{mn}^b)(v_{mm}^c + v_{nn}^c)\right]. \quad (6)$$

For the model in Eq. (1), we obtain quantized values

$$\sigma_{abc}^{0} = i\epsilon_{abc}s_\mu\chi\frac{e^2}{3h}$$
$$\times\begin{cases}0 & j=1/2,\\\Theta(\hbar\omega-|\mu|) & j=1,\\3\left[\Theta\left(\hbar\omega-\frac{3|\mu|}{2}\right)-\Theta(\hbar\omega-2|\mu|)\right] & j=3/2,\end{cases} \quad (7)$$

where $s_\mu = \mu/|\mu|$ [Fig. 3(a)]. The Chern number origin of the quantization is manifested in the expression of the nonvanishing value $\sigma_{xyz}^{0} = -is_\mu c_{2j+j}e^2(6h)^{-1}$ $|(1+v_{2j}/v_{2j+1})/(1-v_{2j}/v_{2j+1})|$, where $c_{2j+1} = -(2\pi)^{-1}\oint d\mathbf{S}\cdot\mathbf{F}_{2j+j} = -2\chi j$ is the outward Berry flux of the topmost band, i.e., band $2j+1$ (see Supplemental Material [28]). We note that the velocity ratio takes a universal value independent of material specifics, $v_{2j}/v_{2j+1} = -1, 0$, and $1/3$ for $j = 1/2, 1$, and $3/2$, only when the effective Hamiltonian has isotropy, which requires specific space group symmetries as we discuss above.

The isotropic linearly dispersing Weyl fermion does not show circular dichroism from the Fermi sea [42]. This is because of the constraint from CP symmetry that imposes $B_{mn}^{ab} = 0$ and $v_{mm}^a + v_{nn}^a = 0$ between CP-related states m and n, where C is particle-hole conjugation, and P is spatial inversion [28]. The nontrivial circular dichroism of multifold fermions is due to CP-asymmetric optical excitations which generate the net change of the orbital magnetic
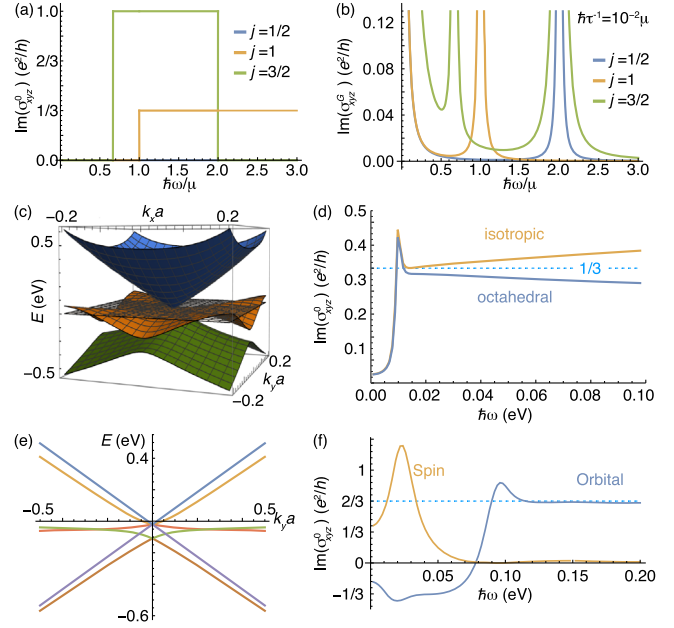

FIG. 3. The imaginary part of σ_{xyz} of a pseudospin-j fermion. (a),(b) Spinless linearly dispersing fermion. (a) Fermi sea contribution σ_{xyz}^{0} and (b) Fermi surface contribution σ_{xyz}^{G} of the linearly dispersing model in Eq. (1) without quadratic terms. While we take $\omega\tau \to \infty$ in (a), we introduce a finite relaxation time in (b). We take $\mu > 0$ for all plots. (c),(d) Band structure and σ_{xyz}^{0} with quadratic terms in Eq. (10). $\mu = 0.01$ eV, $A = 1.07\tilde{a}^2$ eV, $B = -1.72\tilde{a}^2$ eV, $C = 3.26\tilde{a}^2$ eV, and $\hbar v = 1.79\tilde{a}$ eV, where $\tilde{a} = a_{\text{CoSi}}/(2\pi)$, $a_{\text{CoSi}} = 4.45$ Å is the lattice constant of CoSi, $\hbar\tau^{-1} = 1$ meV. The transparent plane in (c) shows the Fermi level. The orange curve in (d) shows the isotropic case ($B = C = 0$ with other parameters kept unchanged) for comparison. (e),(f) Band structure and σ_{xyz}^{0} with spin-orbit coupling in Eq. (11). $w = 30a$ meV, $\Delta = 30$ meV, and $\hbar\tau^{-1} = 10$ meV. In (f), the spin part is due to spin magnetic moment, and the orbital part refers to the other contributions.

moment. This favors the absorption of one particular circular polarization of light to the other polarization.

Let us consider shining linearly polarized or unpolarized light. Then, the incident intensity is the same for L/R helicity on average. The transmitted light intensity after propagation of the distance d within the material is $I_{L/R} = 2^{-1}I_0|\exp(2\pi in_{L/R}d/\lambda)|^2$ for L/R helicity, where I_0 is the incident light intensity. The transmissive circular dichroism is defined by

$$\text{CD} \equiv \frac{I_L - I_R}{I_L + I_R} = \tanh\left(\chi s_\mu\frac{4\pi\alpha N_j}{3}\frac{d}{\lambda}\right), \quad (8)$$

where $\alpha = \mu_0 ce^2/2h$ is the fine structure constant.

In the clean limit, the Fermi surface part does not contribute to the circular dichroism because it is real valued, where

$$\sigma_{abc}^{G} = \epsilon_{abc}\chi\frac{e^2}{3\pi h}\frac{\mu}{\hbar\omega}\left[\frac{\mu^2 - 3j^2(\hbar\omega)^2/2}{\mu^2 - j^2(\hbar\omega)^2} + f_j\right], \quad (9)$$

and $f_{1/2} = f_1 = 0$, and $f_{3/2} = 7[\mu^2 - 3(\hbar\omega)^2/8]/[\mu^2 - (\hbar\omega)^2/4]$. But this contributes to the circular dichroism when there is a finite relaxation and is proportional to τ^{-1}. Figure 3(b) shows the case with $\hbar\tau^{-1} = 0.01\mu$.

Effect of quadratic dispersion and spin-orbit coupling.—To see the effect of $O(k^2)$ terms, we consider $H = H_0 + H_1$ of a threefold fermion with an additional quadratic Hamiltonian allowed by octahedral symmetry:

$$H_1 = \begin{pmatrix} Xk^2 - 2Ck_z^2 & Bk_yk_z & Bk_zk_x \\ Bk_yk_z & Xk^2 - 2Ck_x^2 & Bk_xk_y \\ Bk_zk_x & Bk_xk_y & Xk^2 - 2Ck_y^2 \end{pmatrix}, \quad (10)$$

where $X = A + 2C/3$, and $\mathbf{J} = \{-\lambda_2, \lambda_5, -\lambda_7\}$ for H_0, and λ_i is the Gell-Mann matrix [13].

Figure 3(c) shows the band structure with quadratic terms included. We take $\mu = 0.1$ eV and the model parameters for CoSi derived in Ref. [13], which are $A = 1.07\tilde{a}^2$ eV, $B = -1.72\tilde{a}^2$ eV, $C = 3.26\tilde{a}^2$ eV, and $\hbar v = 1.79\tilde{a}$ eV, where $\tilde{a}$ has the dimension of length ($\tilde{a} = a_{CoSi}/2\pi$, where $a_{CoSi} = 4.45$ Å is the lattice constant of CoSi).

When the quadratic terms are included, the value of $Im(\sigma_{xyz}^0)$ deviates from the quantized plateau [Fig. 3(d)]. The deviation originates from the momentum dependence of the velocities of bands [28], and the effect of selection-rule-breaking transitions is negligible (less than 1%). Therefore, an isotropic quadratic dispersion that preserves the selection rule can lead to a comparable deviation from the quantization [orange curve in Fig. 3(d)].

The effect of spin-orbit coupling is twofold. One is the spin-orbit splitting of the band structure, and the other is contribution from the spin magnetic moment. The former effect is absent in the case where Eq. (1) is realized in the presence of spin-orbit coupling. Here, we consider the case of a threefold fermion realized in each spin sector in the absence of spin-orbit coupling, with application to CoSi in mind. In this case, the spin-orbit coupling up to linear order in k is given by

$$H_{SOC} = \mathbf{s} \cdot (w\mathbf{k} + \Delta\mathbf{J}), \quad (11)$$

where $s_{i=x,y,z}$ is the spin Pauli matrix. For a threefold (per spin) fermion, this splits the sixfold (including spin) degeneracy into fourfold and twofold degenerate points by $\delta E_{SOC} = 3\Delta$ [Fig. 3(e)]. Figure 3(f) shows that the circular dichroism approaches to the quantized value as the photon energy becomes larger than δE_{SOC}. The effect of spin magnetic moment is negligible in the quantized regime.

Chiral threefold semimetal CoSi.—We now turn the discussion toward material-specific DFT-based calculations to test our model analysis. We focus on the transition metal monosilicide family of materials CoSi, which crystalizes in the B20 cubic structure [43,44]. The crystal structure is chiral, and it belongs to the $P2_13$ space group (SG198); it lacks an inversion, mirror, and rotoinversion symmetry. The structural chirality and the octahedral symmetries lead to various types of multifold fermions in these systems [21,43–45]. Specifically, in the absence of spin-orbit interaction, CoSi host a threefold degenerate nodal point at the zone center and double Weyl fermion state at the corner of the cubic BZ [Fig. 4(a)].

We compute $Im(\sigma_{xyz}^0)$ for CoSi using the Wannier function-based tight-binding model (see Supplemental Material for details [28]). The chemical potential (indicated by the green dashed line) is set to be slightly above the threefold degenerate crossing point to ensure full occupancy of the flat band around the Γ point. The tuning of the chemical potential has been experimentally achieved recently in RhSi via Ni doping [46]. As shown in Fig. 4(c), the calculated $Im(\sigma_{xyz}^0)$ results strongly support our low energy model analysis. Specifically, we found that in CoSi, the $Im(\sigma_{xyz}^0)$ starts from a finite value for low photon energy and it quickly approaches the quantized value $e^2/3h$, developing a plateaulike region for $50 \lesssim \hbar\omega \lesssim 200$ meV. In this region, the optical transitions involving the threefold fermion around the Γ point plays the important role. The small deviation from the quantized value is attributed to the presence of quadratic band dispersion, and it supports our model analysis. For $\hbar\omega \gtrsim 200$ meV, the optical transitions
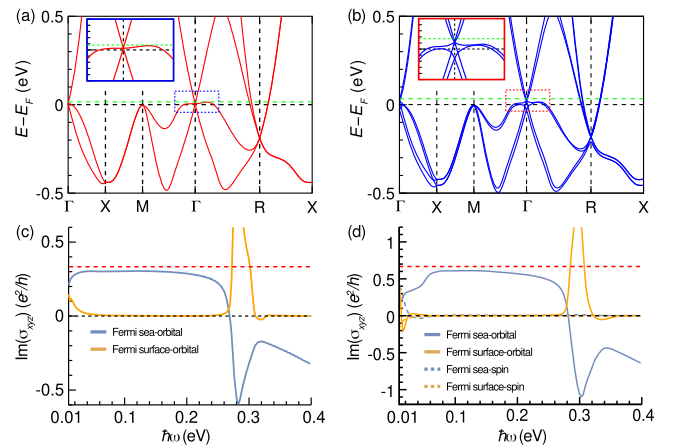

FIG. 4. *Ab initio* calculations for threefold semimetal CoSi based on density functional theory. (a),(b) Band structure. (a) Without and (b) with spin-orbit coupling. The insets show the band structure near the Γ point. The horizontal green dashed line denotes the chemical potential used for computing the σ_{xyz}^0 and σ_{xyz}^G. (c),(d) The imaginary parts of Fermi-sea (σ_{xyz}^0) and Fermi-surface (σ_{xyz}^G) contributions (c) without and (d) with spin-orbit coupling. $\hbar\tau^{-1} = 1$ meV.

involving the states around the R point become important, and consequently, the $\mathrm{Im}(\sigma^0_{xyz})$ changes sign, as it strongly deviates from the quantized value. For comparison, we also compute the Fermi surface contribution $\mathrm{Im}(\sigma^G_{xyz})$ for CoSi, which was studied in a previous work [11]. In general, $\mathrm{Im}(\sigma^G_{xyz})$ is smaller compared to the $\mathrm{Im}(\sigma^0_{xyz})$, and its value depends strongly on the relaxation time, and in the clean limit $\omega\tau \gg 1$. This Fermi surface contribution should be negligible in the quantized region.

We further consider the effect of spin-orbit coupling in Figs. 4(b) and 4(d). Consistent with model analysis, approximate quantization of $\mathrm{Im}(\sigma^0_{xyz})$ still holds true even after including the effect of spin-orbit coupling, and the spin magnetic moment contributes negligibly compared to the orbital part in the plateau region.

We also explored other material candidates in this family, including RhSi, and PtAl (see Supplemental Material [28] and [47,48]). Our analysis suggests that in the absence of spin-orbit coupling, the approximate quantization of $\mathrm{Im}(\sigma^0_{xyz})$ holds true both in RhSi and PtAl. However, due to the presence of large spin-orbit coupling in these compounds, the $\mathrm{Im}(\sigma^0_{xyz})$ deviates from the quantized value. Interestingly, this deviation is still approximately within 10% for RhSi and 20% for PtAl, despite the spin-orbit coupling being significantly stronger compared to CoSi.

Conclusion.—Our analysis establishes that topological circular dichroism is the unique feature of multifold fermions in the k dot p regime. Thin films will be ideal for an observation of this effect because transmitted light intensity is exponentially suppressed in bulk samples. Topological circular dichroism is similar to the quantized absorption in graphene [49] because it requires linear dispersion. The quantization is expected to be robust as long as photon energy is much larger than thermal energy. However, disorder and interaction effects can give deviations from quantized optical responses [50,51], in contrast to the quantum Hall effect. We leave detailed analysis of these effects for future studies.

*junyeongahn@fas.harvard.edu
†b.ghosh@northeastern.edu

[1] N. P. Huck, W. F. Jager, B. De Lange, and B. L. Feringa, Dynamic control and amplification of molecular chirality by circular polarized light, Science **273**, 1686 (1996).

[2] J. Bailey, A. Chrysostomou, J. Hough, T. Gledhill, A. McCall, S. Clark, F. Ménard, and M. Tamura, Circular polarization in star-formation regions: Implications for biomolecular homochirality, Science **281**, 672 (1998).

[3] B. L. Feringa and R. A. Van Delden, Absolute asymmetric synthesis: The origin, control, and amplification of chirality, Angew. Chem., Int. Ed. **38**, 3418 (1999).

[4] A. Malashevich and I. Souza, Band theory of spatial dispersion in magnetoelectrics, Phys. Rev. B **82**, 245118 (2010).

[5] S. Zhong, J. E. Moore, and I. Souza, Gyrotropic Magnetic Effect and the Magnetic Moment on the Fermi Surface, Phys. Rev. Lett. **116**, 077201 (2016).

[6] S.-Y. Xu, Q. Ma, Y. Gao, A. Kogar, A. Zong, A. M. Mier Valdivia, T. H. Dinh, S.-M. Huang, B. Singh, C.-H. Hsu *et al.*, Spontaneous gyrotropic electronic order in a transition-metal dichalcogenide, Nature (London) **578**, 545 (2020).

[7] F. de Juan, A. G. Grushin, T. Morimoto, and J. E. Moore, Quantized circular photogalvanic effect in Weyl semimetals, Nat. Commun. **8**, 15995 (2017).

[8] J. Orenstein, J. Moore, T. Morimoto, D. Torchinsky, J. Harter, and D. Hsieh, Topology and symmetry of quantum materials via nonlinear optical responses, Annu. Rev. Condens. Matter Phys. **12**, 247 (2021).

[9] Q. Ma, A. G. Grushin, and K. S. Burch, Topology and geometry under the nonlinear electromagnetic spotlight, Nat. Mater. **20**, 1601 (2021).

[10] P. Bhalla, K. Das, D. Culcer, and A. Agarwal, Resonant Second-Harmonic Generation as a Probe of Quantum Geometry, Phys. Rev. Lett. **129**, 227401 (2022).

[11] F. Flicker, F. de Juan, B. Bradlyn, T. Morimoto, M. G. Vergniory, and A. G. Grushin, Chiral optical response of multifold fermions, Phys. Rev. B **98**, 155145 (2018).

[12] D. Rees, K. Manna, B. Lu, T. Morimoto, H. Borrmann, C. Felser, J. Moore, D. H. Torchinsky, and J. Orenstein, Helicity-dependent photocurrents in the chiral Weyl semimetal RhSi, Sci. Adv. **6**, eaba0509 (2020).

[13] Z. Ni, K. Wang, Y. Zhang, O. Pozo, B. Xu, X. Han, K. Manna, J. Paglione, C. Felser, A. G. Grushin *et al.*, Giant topological longitudinal circular photo-galvanic effect in the chiral multifold semimetal CoSi, Nat. Commun. **12**, 1 (2021).

[14] B. Bradlyn, J. Cano, Z. Wang, M. G. Vergniory, C. Felser, R. J. Cava, and B. A. Bernevig, Beyond Dirac and Weyl fermions: Unconventional quasiparticles in conventional crystals, Science **353**, aaf5037 (2016).

[15] G. Chang, B. J. Wieder, F. Schindler, D. S. Sanchez, I. Belopolski, S.-M. Huang, B. Singh, D. Wu, T.-R. Chang,

T. Neupert *et al.*, Topological quantum properties of chiral crystals, Nat. Mater. **17**, 978 (2018).

[16] H. B. Nielsen and M. Ninomiya, A no-go theorem for regularizing chiral fermions, Technical Report No. 2-3, 1981, 10.1016/0370-2693(81)91026-1.

[17] S. Sekh and I. Mandal, Circular dichroism as a probe for topology in three-dimensional semimetals, Phys. Rev. B **105**, 235403 (2022).

[18] I. Mandal, Signatures of two- and three-dimensional semimetals from circular dichroism, Int. J. Mod. Phys., 2450216 (2023).

[19] G. Chang, S.-Y. Xu, B. J. Wieder, D. S. Sanchez, S.-M. Huang, I. Belopolski, T.-R. Chang, S. Zhang, A. Bansil, H. Lin *et al.*, Unconventional Chiral Fermions and Large Topological Fermi Arcs in RhSi, Phys. Rev. Lett. **119**, 206401 (2017).

[20] P. Tang, Q. Zhou, and S.-C. Zhang, Multiple Types of Topological Fermions in Transition Metal Silicides, Phys. Rev. Lett. **119**, 206402 (2017).

[21] Z. Rao, H. Li, T. Zhang, S. Tian, C. Li, B. Fu, C. Tang, L. Wang, Z. Li, W. Fan *et al.*, Observation of unconventional chiral fermions with long Fermi arcs in CoSi, Nature (London) **567**, 496 (2019).

[22] D. S. Sanchez, I. Belopolski, T. A. Cochran, X. Xu, J.-X. Yin, G. Chang, W. Xie, K. Manna, V. Süß, C.-Y. Huang *et al.*, Topological chiral crystals with helicoid-arc quantum states, Nature (London) **567**, 500 (2019).

[23] B. Xu, Z. Fang, M.-Á. Sánchez-Martínez, J. W. Venderbos, Z. Ni, T. Qiu, K. Manna, K. Wang, J. Paglione, C. Bernhard *et al.*, Optical signatures of multifold fermions in the chiral topological semimetal CoSi, Proc. Natl. Acad. Sci. U.S.A. **117**, 27104 (2020).

[24] M.-Á. Sánchez-Martínez, F. de Juan, and A. G. Grushin, Linear optical conductivity of chiral multifold fermions, Phys. Rev. B **99**, 155145 (2019).

[25] J. Cano, B. Bradlyn, and M. G. Vergniory, Multifold nodal points in magnetic materials, APL Mater. **7**, 101125 (2019).

[26] Ó. Pozo and I. Souza, Multipole theory of optical spatial dispersion in crystals, SciPost Phys. **14**, 118 (2023).

[27] P. Goswami and S. Tewari, Chiral magnetic effect of weyl fermions and its applications to cubic noncentrosymmetric metals, arXiv:1311.1506.

[28] See Supplemental Material at http://link.aps.org/supplemental/10.1103/PhysRevLett.131.116603 for more details of the symmetry analysis, model calculations, and first-principles calculations, which includes Refs. [29–41].

[29] Y. Gao and D. Xiao, Nonreciprocal Directional Dichroism Induced by the Quantum Metric Dipole, Phys. Rev. Lett. **122**, 227402 (2019).

[30] M. F. Lapa and T. L. Hughes, Semiclassical wave packet dynamics in nonuniform electric fields, Phys. Rev. B **99**, 121111(R) (2019).

[31] J. Ma and D. A. Pesin, Chiral magnetic effect and natural optical activity in metals with or without Weyl points, Phys. Rev. B **92**, 235205 (2015).

[32] J. Ahn and N. Nagaosa, Theory of optical responses in clean multi-band superconductors, Nat. Commun. **12**, 1617 (2021).

[33] J. Ahn and N. Nagaosa, Many-body selection rule for quasiparticle pair creations in centrosymmetric superconductors, arXiv:2108.04846.

[34] G. Kresse and J. Furthmüller, Efficient iterative schemes for *ab initio* total-energy calculations using a plane-wave basis set, Phys. Rev. B **54**, 11169 (1996).

[35] G. Kresse and D. Joubert, From ultrasoft pseudopotentials to the projector augmented-wave method, Phys. Rev. B **59**, 1758 (1999).

[36] J. P. Perdew, K. Burke, and M. Ernzerhof, Generalized Gradient Approximation Made Simple, Phys. Rev. Lett. **77**, 3865 (1996).

[37] N. Marzari and D. Vanderbilt, Maximally localized generalized Wannier functions for composite energy bands, Phys. Rev. B **56**, 12847 (1997).

[38] N. Marzari, A. A. Mostofi, J. R. Yates, I. Souza, and D. Vanderbilt, Maximally localized Wannier functions: Theory and applications, Rev. Mod. Phys. **84**, 1419 (2012).

[39] J. Ibañez-Azpiroz, S. S. Tsirkin, and I. Souza, *Ab initio* calculation of the shift photocurrent by Wannier interpolation, Phys. Rev. B **97**, 245143 (2018).

[40] C. Wang, X. Liu, L. Kang, B.-L. Gu, Y. Xu, and W. Duan, First-principles calculation of nonlinear optical responses by Wannier interpolation, Phys. Rev. B **96**, 115147 (2017).

[41] S. S. Tsirkin, P. A. Puente, and I. Souza, Gyrotropic effects in trigonal tellurium studied from first principles, Phys. Rev. B **97**, 035158 (2018).

[42] P. Goswami, G. Sharma, and S. Tewari, Optical activity as a test for dynamic chiral magnetic effect of Weyl semimetals, Phys. Rev. B **92**, 161110(R) (2015).

[43] P. Tang, Q. Zhou, and S.-C. Zhang, Multiple Types of Topological Fermions in Transition Metal Silicides, Phys. Rev. Lett. **119**, 206402 (2017).

[44] D. Takane, Z. Wang, S. Souma, K. Nakayama, T. Nakamura, H. Oinuma, Y. Nakata, H. Iwasawa, C. Cacho, T. Kim, K. Horiba, H. Kumigashira, T. Takahashi, Y. Ando, and T. Sato, Observation of Chiral Fermions with a Large Topological Charge and Associated Fermi-Arc Surface States in CoSi, Phys. Rev. Lett. **122**, 076402 (2019).

[45] D. Dutta, B. Ghosh, B. Singh, H. Lin, A. Politano, A. Bansil, and A. Agarwal, Collective plasmonic modes in the chiral multifold fermionic material CoSi, Phys. Rev. B **105**, 165104 (2022).

[46] T. A. Cochran *et al.*, Visualizing Higher-Fold Topology in Chiral Crystals, Phys. Rev. Lett. **130**, 066402 (2023).

[47] N. B. M. Schröter, D. Pei, M. G. Vergniory, Y. Sun, K. Manna, F. de Juan, J. A. Krieger, V. Süss, M. Schmidt, P. Dudin, B. Bradlyn, T. K. Kim, T. Schmitt, C. Cacho, C. Felser, V. N. Strocov, and Y. Chen, Chiral topological semimetal with multifold band crossings and long Fermi arcs, Nat. Phys. **15**, 759 (2019).

[48] H. Li, S. Xu, Z.-C. Rao, L.-Q. Zhou, Z.-J. Wang, S.-M. Zhou, S.-J. Tian, S.-Y. Gao, J.-J. Li, Y.-B. Huang, H.-C. Lei,

H.-M. Weng, Y.-J. Sun, T.-L. Xia, T. Qian, and H. Ding, Chiral fermion reversal in chiral crystals, Nat. Commun. **10,** 5505 (2019).

[49] R. R. Nair, P. Blake, A. N. Grigorenko, K. S. Novoselov, T. J. Booth, T. Stauber, N. M. Peres, and A. K. Geim, Fine structure constant defines visual transparency of graphene, Science **320,** 1308 (2008).

[50] A. Avdoshkin, V. Kozii, and J. E. Moore, Interactions Remove the Quantization of the Chiral Photocurrent at Weyl Points, Phys. Rev. Lett. **124,** 196603 (2020).

[51] I. Mandal, Effect of interactions on the quantization of the chiral photocurrent for double-Weyl semimetals, Symmetry **12,** 919 (2020).